RESEARCH ARTICLE

Engineering the modulation of the active sites and pores of pristine metal–organic frameworks for high-performance sodium-ion storage†

Wei Shuang, Ya Wang, Fuyou Chen, Yujun Wu, Zhengyu Bai* and Lin Yang 🔟 *

Metal–organic framework materials have numerous significant merits for use as electrodes in sodium-ion batteries, such as multiple active sites and porous structures. However, the masked active sites and pores limit their performances. Herein, we rationally selected Ni-HHTP (HHTP = 2,3,6,7,10,11-hexahydroxytriphenylene) with a stable structure, and adopted thermal treatment prior to its carbonization to open blocked pores and expose multiple active sites. As expected, after thermal treatment at a low temperature of 250 °C, the obtained Ni-HHTP-250 sample still retained the intrinsic crystal skeleton and crystal type, and exposed more actives sites and pores than those of pristine Ni-HHTP. The obtained Ni-HHTP-250 as an electrode material for sodium-ion batteries exhibits a large reversible discharge capacity of 420 mA h g^{-1} at 0.1 A g^{-1} along with a fine rate capability of 200 mA h g^{-1} at 2.0 A g^{-1}. Mechanism studies show that both the Ni ions and organic ligands in the Ni-HHTP-250 sample are active sites. The H_2O molecules and the −OH subgroups in the pores masking the active site can be removed after heat treatment. Hence, the excellent electrochemical performance is largely due to the open porous structure and exposed active sites, resulting in rapid Na^+ diffusion and relatively high electronic conductivity. This work offers an innovative idea for preparing high-performance electrodes of metal-ion batteries.

Introduction

With the wide application of clean energy, the global market demand for energy storage is facing a rapid increase. In recent years, among many large-scale energy storage technologies, electrochemical energy storage based on battery technology has rapidly developed.[1] Since lithium-ion batteries (LIBs) first commercialized in 1991, rechargeable LIBs have occupied the main market of secondary batteries due to their high energy density and long life.[2] However, with the continuous depletion of lithium resources and the increasing price of LIBs in the near future,[3–6] developing other batteries with high energy and low cost is very urgent. In contrast, sodium is rich in resources and low-cost on the earth.[7] In addition, LIBs and sodium-ion batteries (SIBs) show the same working principle.[8] Therefore, SIBs are the most appropriate substitutes to LIBs. Unfortunately, most advanced electrode materials in LIBs

exhibit inferior electrochemical performance in SIBs because of the fact that the radius of sodium ions (∼1.02 Å) is larger than that of lithium ions (∼0.68 Å).[9] Hence, it is very critical to explore appropriate electrodes for the application of SIBs.

Metal–organic frameworks (MOFs), as inorganic–organic hybrid materials, are composed of metal nodes and organic ligands through coordination bonds.[10,11] MOFs have the advantages of tunable porosities and compositions as well as remarkable specific surface areas,[12–14] which enable the application of MOFs extensively in gas adsorption and separation,[15,16] drug delivery,[17] molecular sensing[18] and so on. In recent years, MOFs and their derivatives have attracted great attention for their applications in energy storage and conversion.[19,20] However, in the SIB field, a small number of MOFs have been used as electrodes.[21–24] In contrast, MOF derivatives are widely used in SIBs, such as carbon materials,[25] metal oxides,[26] metal sulfides, phosphides, and selenides.[27–29] Only a few pristine MOFs are used as electrodes for SIBs because there are improvements in some aspects of MOFs: (1) coordination bonds between metal ions and organic ligands are needed to strengthen to increase the cycling stability; (2) it is necessary to enhance the electronic conductivity to increase the electrochemical activity and reaction kinetics; and (3) the solvent molecules in channels and pores need to be removed to expose clogged pores and active sites. In addition, the

Collaborative Innovation Center of Henan Province for Green Manufacturing of Fine Chemicals, Key Laboratory of Green Chemical Media and Reactions, Ministry of Education, School of Chemistry and Chemical Engineering, Henan Normal University, Xinxiang, Henan 453007, P. R. China. E-mail: baizhengyu@htu.edu.cn, yanglin@htu.edu.cn

mechanism of charge/discharge reaction remains to be studied, for example, whether metal ions participate in the redox reaction, and what role do organic ligands play. Thus, there is an urgent need to obtain MOFs with strong coordination bonds and opened pores. Furthermore, it is necessary to enhance the electronic conductivity and to understand the reaction mechanism.

Integration of the high stability, high electronic conductivity and high density of redox-active centers in MOFs is challenging but promising. By extending conjugation, the metal and the ligands can form large delocalized systems to increase the stability and conductivity of MOFs.[30] Through post-treatment (recombination with conductive materials and calcination below the carbonization temperature), the electrical conductivity and stability of MOFs can be further enhanced, and active sites can be exposed.[31] In order to meet the above challenges, we used 2,3,6,7,10,11-HHTP as a ligand for constructing Ni-HHTP as an electrode material in SIBs. The hydroxyl groups in HHTP are conducive to forming robust coordination bonds with Ni ions,[32] resulting in an increase of the orbital overlap between Ni^{2+} and organic ligands, which not only can facilitate charge transfer but also can boost effective charge delocalization for energy storage. In order to open blocked pores, expose plentiful active sites and strengthen the stability of the structure, thermal treatment prior to decomposition was performed. The heat treatment can make organic ligands stack to different degrees. The stacking of organic ligands will result in the appearance of large pores. The H_2O molecules and the –OH subgroups occupying the pores can be removed after heat treatment, as well as the stacking of organic ligands resulting in larger pores, which will facilitate the exposure of active sites.

The obtained Ni-HHTP-250 sample exhibits a remarkable discharge capacity of 420 mA h g^{-1} at 0.1 A g^{-1} along with a good rate capability of 200 mA h g^{-1} at 2.0 A g^{-1} and outstanding cycling stability even at high rates. The studies of the charge/discharge mechanism reveal that both the inorganic metal ions and organic ligands are active sites, and the H_2O molecules in the pores and the –OH subgroups masking the active site can be removed after heat treatment. Hence, the remarkable electrochemical performance is largely due to the open porous structure and exposed active sites, resulting in rapid Na^+ diffusion and a relatively high electronic conductivity. This work offers a new idea for constructing MOFs with a large number of active sites, enhanced electronic conductivity and stability for high-performance electrodes for metal-ion batteries.

Experimental

Materials

Nickel acetate tetrahydrate ($Ni(OAc)_2 \cdot 4H_2O$) was purchased from Aladdin and 2,3,6,7,10,11-hexahydroxytriphenylene (HHTP) was purchased from Macklin. All reagents were purchased commercially and used without further purification.

Preparation of Ni-HHTP-250

Ni-HHTP was synthesized according to the reported methods.[33] Subsequently, the as-prepared Ni-HHTP MOF was annealed at 250 °C for 2 h under an argon atmosphere at 5 °C min^{-1}.

In a similar way, Ni-HHTP-160, Ni-HHTP-340 and Ni-HHTP-500 were synthesized at 160 °C, 340 °C and 500 °C, respectively.

Characterization

The crystal structures of these samples were determined by powder X-ray diffraction (PXRD, Bruker D8 ADVANCE, Berlin German) with a graphite monochromatized Cu Kα radiation source (λ = 0.15406 nm). The morphologies and structures of the samples were characterized using a scanning electron microscope (FESEM, Hitachi, SU8010, Japan) and a transmission electron microscope (TEM, Hitachi, JEOL-JEM2100F). The compositions and chemical states were determined using an X-ray photoelectron spectroscopy spectrometer (XPS, Thermo Scientific Escalab 220i-XL, Thermo Scientific, USA). Fourier-transform infrared (FT-IR) spectra were obtained using a FT-IR spectrometer (FTS-40). The Brunauer–Emmett–Teller (BET) surface area and pore size distribution data were collected by N_2 adsorption/desorption tests at 77 K using a Micromeritics ASAP 2460. The mass loss was analyzed by thermogravimetry with mass spectrometry (TG-MS, STA449F3-QMS403D, Germany).

Electrochemical measurements

To prepare the working electrodes, the active material (Ni-MOF, 70 wt%), Ketjen black (KB, 20 wt%), and polyvinylidene fluoride (PVDF, 10 wt%) were mixed using N-methyl-2-pyrrolidone (NMP) to form a uniform slurry. Then, the slurry was coated on Cu foil and dried in a vacuum oven at 110 °C for 12 h. The thickness of the electrode on the Cu foil was about 150 μm and the mass loading of the Ni-MOF was about 0.8–1.2 mg cm^{-2}. The Ni-MOF electrode, counter electrode (sodium metal), current collectors (Cu foils), and separator (Whatman GF/F) were used to assemble 2032 coin-type cells in a glove box filled with an argon atmosphere (H_2O and O_2 levels <0.5 ppm). 1 M $NaClO_4$ dissolved in ethylene carbonate (EC) and diethyl carbonate (DEC) (1 : 1 v/v) was used as the electrolyte. Galvanostatic discharge/charge experiments were performed using a LANDAT test system at room temperature in a voltage range from 0.01 to 3.0 V at different current densities. Cyclic voltammetry (CV) and electrochemical impedance spectroscopy (EIS) were performed using an electrochemical workstation (CHI 660E). The scan rate of CV was from 0.1 to 1 mV s^{-1}. EIS measurements were conducted from 10^5 to 10^{-2} Hz.

Results and discussion

Synthesis and characterization

The synthetic process of the Ni-HHTP-250 sample is shown in Fig. 1. First, Ni-HHTP was synthesized through a hydrothermal method.[33] As shown in Fig. 2b and c, the XRD patterns and
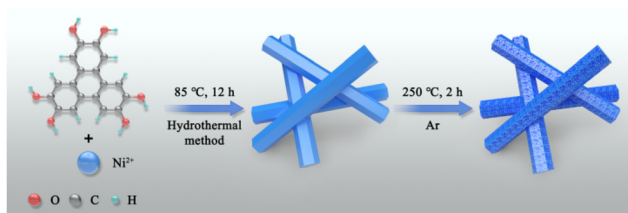
This journal is © the Partner Organisations 2023

Inorg. Chem. Front., 2023, **10**, 396–405 | **397**

Fig. 1 Synthetic diagram of the Ni-HHTP-250 sample.

FT-IR spectra show the successful synthesis of the Ni-HHTP sample.[34] In the FT-IR spectra (Fig. 2c), compared with HHTP, the new stretch at about 1625 cm^{-1} in the Ni-HHTP sample is assigned to C=O. During the coordination of metal ions and organic ligands, a d–π conjugate is formed due to the redistribution and delocalization of electrons, which in this case forms C=O.[35] The d–π conjugate can enhance the stability of MOFs.[36] Then, the Ni-HHTP sample was heated at 250 °C for 2 h under an Ar atmosphere to obtain the Ni-HHTP-250 sample.

The temperature of thermal treatment is based on TG-MS (Fig. 2a). The temperature of thermal treatment is very important for electrochemical performance. The mass loss in the first step between 30 °C and 220 °C is attributed to the release of hydroxyl groups and H_2O molecules in the pores, showing mass signals at 17 (m/z = 17, OH) and 18 (m/z = 18, H_2O). The removal of hydroxyl groups and water molecules in the pores can expose clogged pores and active sites, which facilitates their electrochemical performance as electrode material. The CO_2 (m/z = 44) and C (m/z = 12) signal peaks are detected in the second step between 370 °C and 550 °C, attributed to the

carbonization of Ni-HHTP. According to the test results of TG-MS, the Ni-HHTP sample was calcined below the carbonization temperature. The XRD results show that the Ni-HHTP-250 sample almost retains the original crystal structure of the Ni-HHTP sample. As seen from Fig. 2b, the diffraction peaks at 4.7°, 9.3° and 12.3° of the Ni-HHTP-250 sample basically maintain the characteristic peaks of pristine Ni-HHTP, indicating that the ab plane is stable. The peak intensity at 27.3° of the Ni-HHTP-250 sample is lower than that of pristine Ni-HHTP due to the damage of the c-axis,[37] which further shortens the length of nanorods. Compared with pristine Ni-HHTP, the FT-IR spectrum of the Ni-HHTP-250 sample shows almost no changes (Fig. 2c). The results of XRD and FT-IR spectroscopy suggest that the Ni-HHTP-250 sample still retains the intrinsic crystal skeleton and crystal type of the Ni-HHTP sample. To further describe the new structure and metal–organic interactions of the Ni-HHTP-250 sample, a comparison of the XPS spectra of pristine Ni-HHTP and Ni-HHTP-250 is shown in Fig. S1.† The content of the Ni–O bond in pristine Ni-HHTP is lower than that in Ni-HHTP-250. Because the metal–organic interaction is stronger than that of metal–solvent molecules, the reduction of Ni–O bond content is mainly due to the destruction of coordination between the Ni ions and O atoms in water molecules by heat treatment. The result implies that heat treatment can remove H_2O molecules to expose unsaturated metal sites. For comparison purposes, the XRD patterns and FT-IR spectra of the Ni-HHTP-160 sample and the Ni-HHTP-340 sample were also recorded. The results show that the Ni-HHTP-160 sample and the Ni-HHTP-340 sample also retain the intrinsic crystal skeleton and crystal type of the Ni-HHTP sample (Fig. 2b and c).
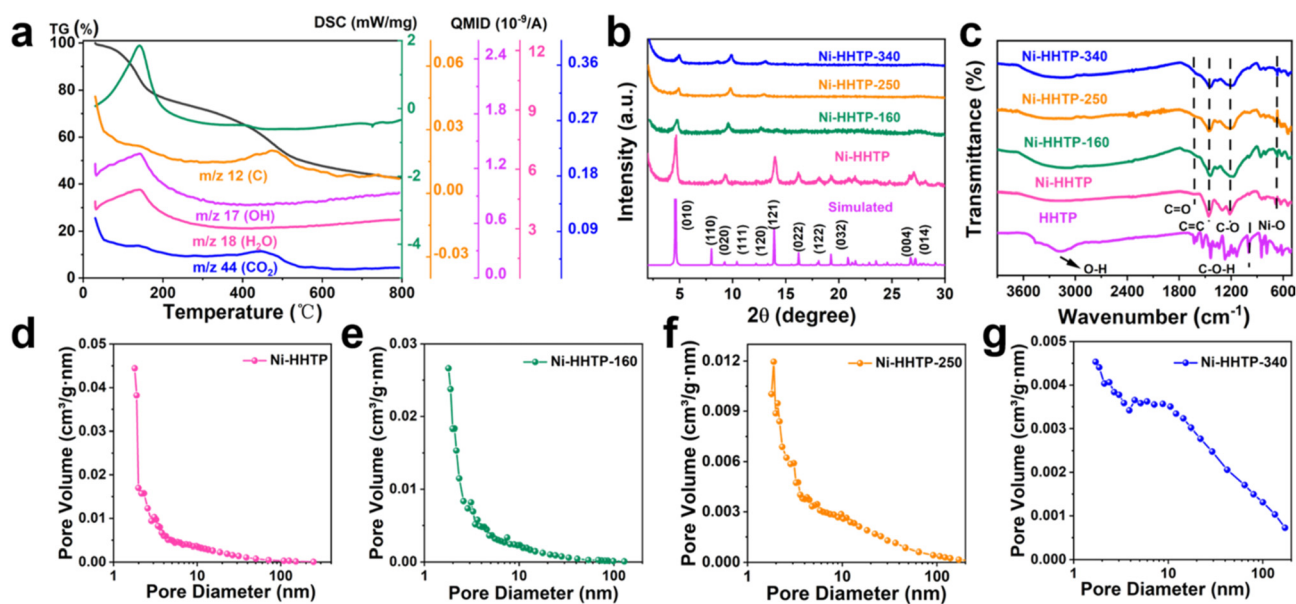

Fig. 2 (a) TG-MS plots of the Ni-HHTP sample during the thermal treatment under nitrogen. (b) XRD patterns of the Ni-HHTP sample, the Ni-HHTP-160 sample, the Ni-HHTP-250 sample and the Ni-HHTP-340 sample. (c) FT-IR spectra of the Ni-HHTP sample, the Ni-HHTP-160 sample, the Ni-HHTP-250 sample and the Ni-HHTP-340 sample. (d–g) Plots of pore-size distribution for the Ni-HHTP sample, the Ni-HHTP-160 sample, the Ni-HHTP-250 sample and the Ni-HHTP-340 sample.

398 | *Inorg. Chem. Front.*, 2023, **10**, 396–405

This journal is © the Partner Organisations 2023

The BET surface areas of the pristine Ni-HHTP sample, the Ni-HHTP-160 sample, the Ni-HHTP-250 sample and the Ni-HHTP-340 sample were tested using nitrogen adsorption and desorption isotherms at 77 k (Fig. S2†). According to the N_2 absorption–desorption curves in Fig. S2,† the pristine Ni-HHTP sample and the calcined Ni-HHTP samples exhibit type IV isotherms. The appearance of hysteresis rings in all the samples indicates the existence of multistage pores. Calculated pore size distributions based on the Barrett–Joyner–Halenda (BJH) method for the pristine Ni-HHTP sample and the calcined Ni-HHTP samples are shown in Fig. 2d–g. With an increase of the calcination temperature, the organic ligands are stacked, so the micropores in the samples decrease, and macropores appear gradually, which will facilitate the exposure of active sites. The Ni-HHTP sample, the Ni-HHTP-160 sample and the Ni-HHTP-340 sample possess two types of pores, while the Ni-HHTP-250 sample possesses three types of pores.

Fig. 2d and e show that the Ni-HHTP sample and the Ni-HHTP-160 sample have micropores and mesopores. The Ni-HHTP-340 sample shows mesopores and macropores (Fig. 2g). Differently, the pore size distributions of Ni-HHTP-250 are micropores, mesopores and macropores (Fig. 2f). In conclusion, the existence of hierarchical pores of the Ni-HHTP-250 sample can provide many active sites and store lots of ions, which are beneficial for the improvement of its electrochemical performance.[38]

The morphologies of the Ni-HHTP sample and the thermally treated samples are shown in Fig. 3. The FESEM and TEM images in Fig. 3a and e indicate that the pristine Ni-HHTP sample exhibits a smooth surface and a uniform nanorod structure of about 1 μm in length and about 50 nm in width. As the calcination temperature increases, the surfaces of the nanorods become rougher and the length of the nanorods becomes shorter (Fig. 3b–d). The FESEM image of the Ni-HHTP-250 sample shows a loofah-like structure with a rough surface, which are about 50 nm in diameter and 200 nm to 1 μm in length (Fig. 3c). The TEM images (Fig. 3g) further confirm that the diameter of the nanorods is about 50 nm and that the rough surface of the nanorods is because of the presence of a porous structure, which could play an important role in sodium ion transport and electrolyte penetration. According to the high-resolution TEM (HRTEM) image in Fig. 3i, a lattice distance of 1.85 nm corresponds to the (010) crystal plane (2θ = 4.7°), which is attributed to the top view of the ab plane.[39] In addition, the corresponding elemental mappings (Fig. 3j) show the uniform distribution of Ni, C and O elements in the nanorods.
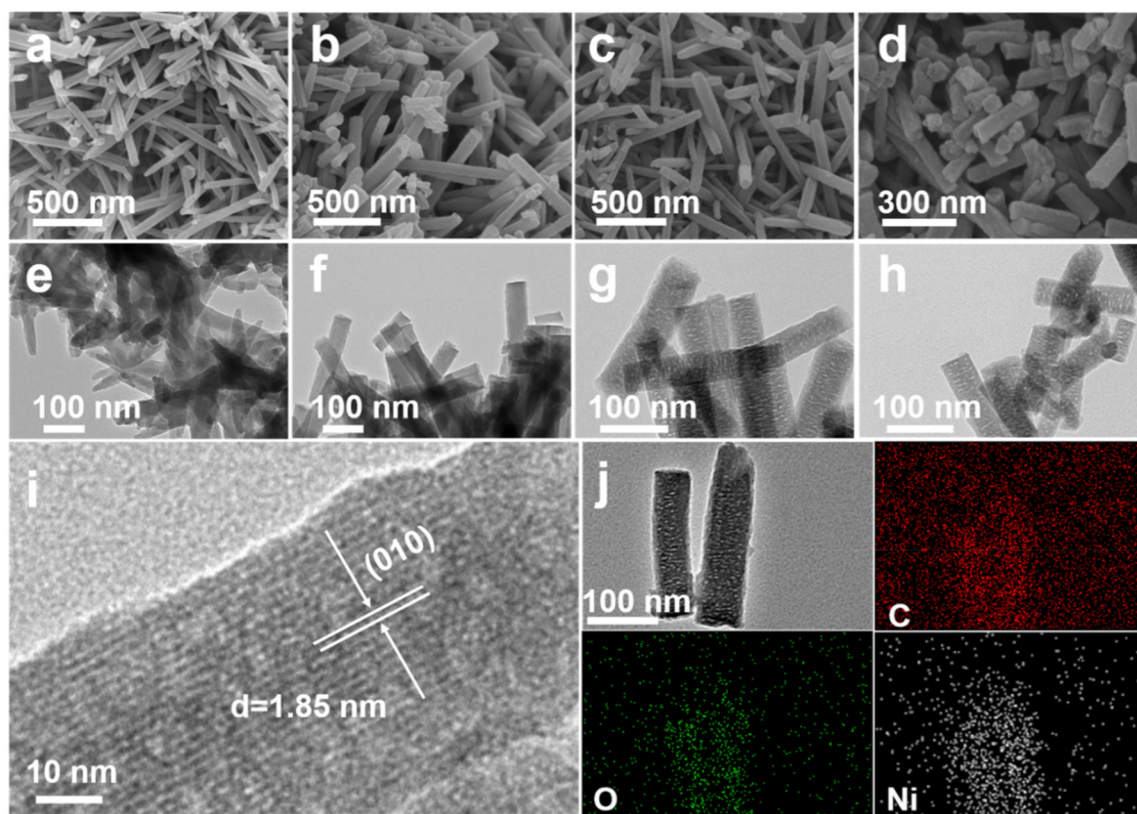

Fig. 3 SEM images of the Ni-HHTP sample (a), the Ni-HHTP-160 sample (b), the Ni-HHTP-250 sample (c) and the Ni-HHTP-340 sample (d). TEM images of the Ni-HHTP sample (e), the Ni-HHTP-160 sample (f), the Ni-HHTP-250 sample (g) and the Ni-HHTP-340 sample (h). (i) HRTEM image of the Ni-HHTP-250 sample. (j) TEM image and the corresponding elemental mappings of the Ni-HHTP-250 sample.

This journal is © the Partner Organisations 2023

Inorg. Chem. Front., 2023, **10**, 396–405 | **399**

Electrochemical performance

The obtained samples show consistent crystallinity after being immersed in an electrolyte for 24 h (Fig. S3†), indicating that the pristine Ni-HHTP sample and the Ni-HHTP samples after thermal treatment are chemically stable, which provides an opportunity for them to be used as stable electrodes in SIBs. The electrochemical performance of the Ni-HHTP-250 sample as an active electrode in SIBs is gauged with a voltage window of 0.01–3.0 V (vs. Na$^+$/Na). The initial five CV curves of the Ni-HHTP-250 sample at a scanning rate of 0.1 mV s^{-1} are presented in Fig. 4a. The peak appearing at about 0.69 V in the first cathodic scan and then disappearing in the following sweeps is due to the formation of a solid electrolyte interphase (SEI) film.[37] Two pairs of peaks at 1.23 V and 1.63 V in the anodic scans and 0.37 V and 0.83 V in the cathodic scans correspond to the reversible redox processes between Ni^{2+} and Ni.[40] The discharge/charge profiles at a current density of 200 mA g^{-1} (Fig. 4b) show an irreversible capacity loss in the first discharge/charge cycle. During the first cycle, the initial discharge and charge capacities are ~1162 and ~450 mA h g^{-1}, respectively, with a first Coulombic efficiency (CE) of ~39%. The capacity loss may derive from the SEI film.[41] In the following cycle of discharge/charge profiles, there is good reversibility. The rate capacity of the Ni-HHTP-250 electrode was obtained at current densities from 0.1 to 2.0 A g^{-1} (Fig. 4c and d). The electrode could maintain the average discharge capacities of ~420, ~340, ~280, ~240, ~215 and ~200 mA h g^{-1} at different current densities of 0.1, 0.2, 0.5, 1.0, 1.5 and 2.0 A g^{-1}, respectively. Inspiringly, when the current densities return to 0.1 and 0.2 A g^{-1}, the reversible capacities recover to ~340 and 304 mA h g^{-1}, respectively. The electrode exhibits a promising cycling performance (Fig. 4e). At a current density of 100 mA g^{-1}, the electrode maintains a reversible capacity of 292 mA h g^{-1} after 100 cycles. At 200 mA g^{-1} and 500 mA g^{-1}, the stable capacities can be maintained at 286 and 257 mA h g^{-1} after 100 cycles, respectively. Due to the presence of hierarchical pores and exposure of the most active sites of the Ni-HHTP-250 sample, it shows the best sodium-ion storage performance among a series of samples at different thermal treatment temperatures. As shown in Fig. S4a and b,† it is evident that the Ni-HHTP-250 sample exhibits the best rate capacity and the highest specific capacity at the same current density compared to the Ni-HHTP sample, the Ni-HHTP-160 sample and the Ni-HHTP-340 sample. By comparison, the specific capacities of the Ni-HHTP sample, the Ni-HHTP-160 sample and the Ni-HHTP-340 sample decrease at a high current density of 500 mA h g^{-1} after 100 cycles, remaining at 187, 153, and 218 mA h g^{-1}, respectively (Fig. S4b†). Moreover, at the same current density, the specific capacity of the Ni-HHTP-250 sample is higher than that of the sample after reaching carbonization temperature (Fig. S5†). At a current density of 500 mA g^{-1}, the Ni-HHTP-500 sample maintains a reversible capacity of 188 mA h g^{-1} after 100 cycles. Compared with other MOF electrode materials reported for SIBs (Fig. 4f), the Ni-HHTP-250 electrode material exhibits an excellent electrochemical performance.[9,23,42–44]
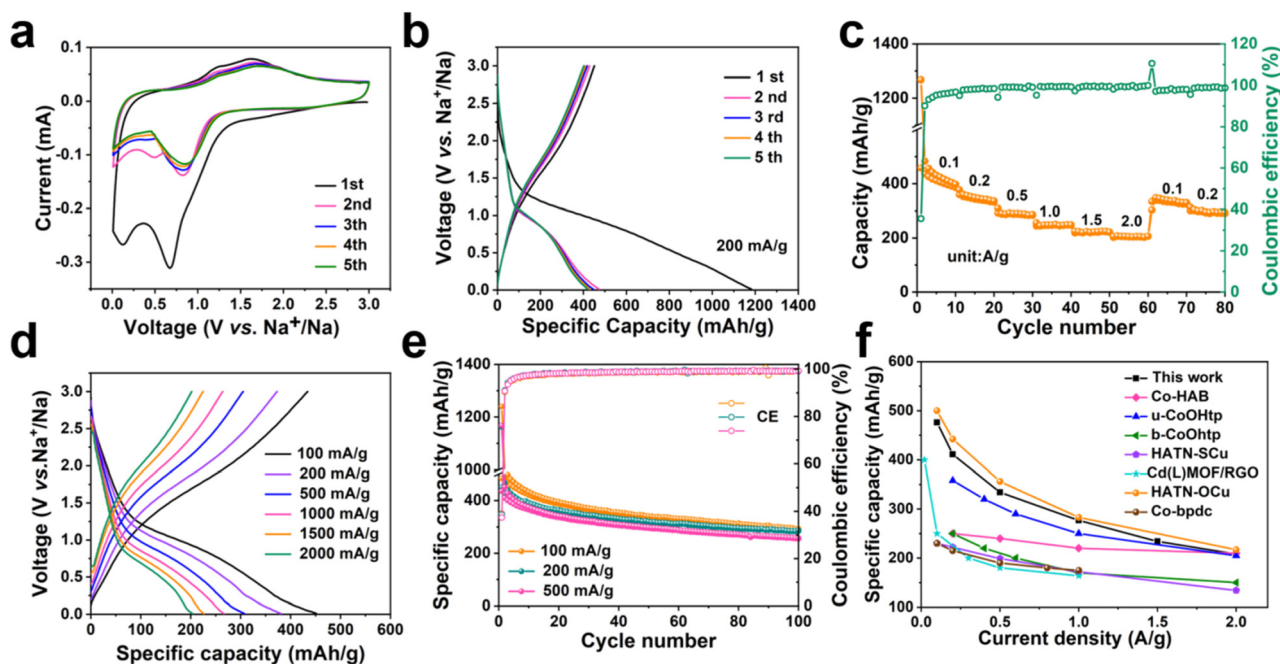

Fig. 4 Electrochemical performance of the Ni-HHTP-250 electrode. (a) CV curves at 0.1 mV s^{-1}. (b) Discharge–charge curves at 200 mA g^{-1}. (c) Rate capacity. (d) Discharge–charge profiles at various current densities. (e) Cycling performance at 100, 200 and 500 mA g^{-1}. (f) Comparison of capacity retention with other reported electrods.

400 | *Inorg. Chem. Front.*, 2023, **10**, 396–405

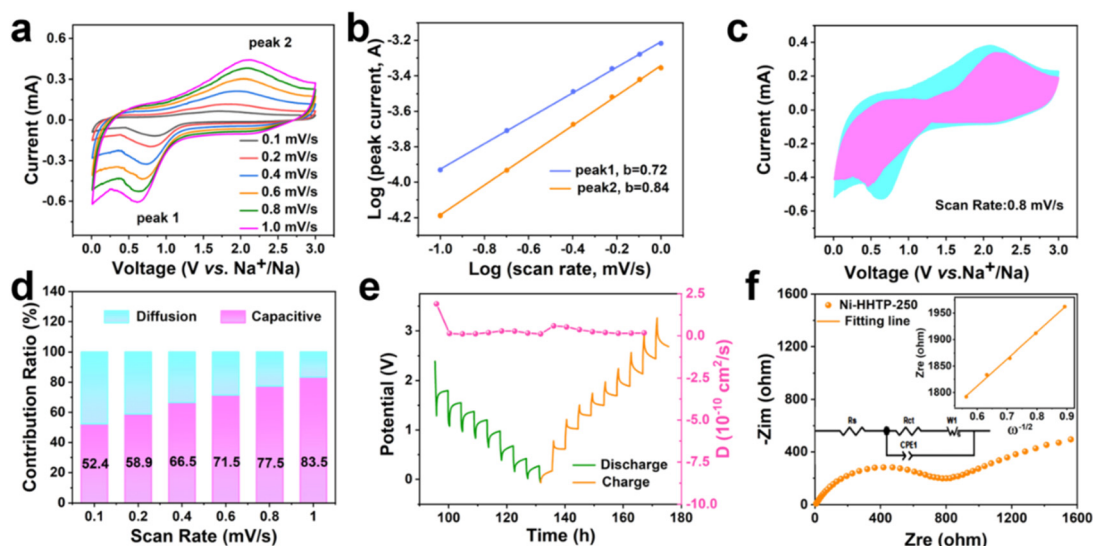This journal is © the Partner Organisations 2023

Fig. 5 Electrochemical kinetics analysis of the Ni-HHTP-250 electrode. (a) CV curves at different scan rates from 0.1 to 1 mV s^{-1}. (b) The corresponding plots of log(i) *vs.* log(v) at peak 1 and peak 2. (c) Capacitance and diffusion-controlled contribution to Na$^+$ ion storage at 0.8 mV s^{-1}. (d) Contribution ratio of capacitive and diffusion-controlled capacities at different scan rates. (e) GITT curves and the derived D_{Na^+} values at various discharge/charge states. (f) Nyquist plot and the corresponding fitted data and an equivalent circuit model for EIS fitting.

CV tests at different scan rates ranging from 0.1 to 1.0 mV s^{-1} are used to further understand the excellent electrochemical kinetics of Ni-HHTP-250 (Fig. 5a). The peak currents (i) and scan rates (v) have the following relationship:[45,46] $i = av^b$, which can be written as: log(i) = b log(v) + log(a). When the b value is 0.5, the electrochemical process is controlled by diffusion. When the b value approaches 1, the electrochemical process is non-Faradaic capacitive-controlled. By fitting the corresponding plots of log(i) *vs.* log(v) (Fig. 5b), the calculated b values are 0.72 and 0.84 in the Ni-HHTP-250 electrode, which indicates that the electrochemical reaction is controlled by a combination of diffusion-controlled and capacitive-controlled processes. Moreover, the capacitive behavior is dominant. The contribution ratio of capacitive-controlled capacity to the total capacity can be calculated using the following equation: $i = k_1v + k_2v^{1/2}$, where i represents the current response, k_1v is the capacitive effect contribution, and $k_2v^{1/2}$ is the diffusion-controlled contribution. According to the calculation results, the contribution ratio of capacitive-controlled capacity is about 77.5% at 0.8 mV s^{-1} (Fig. 5c). As the scan rates increase, the contribution ratios of the capacitive-controlled capacity gradually increase. When the scan rate is up to 1.0 mV s^{-1}, the percentage of the capacitive contribution of the Ni-HHTP-250 electrode reaches 83.5% (Fig. 5d). By comparison, all the percentages of the capacitive contribution of the Ni-HHTP electrode, the Ni-HHTP-160 electrode and the Ni-HHTP-340 electrode are lower than that of the Ni-HHTP-250 electrode at the same scanning rate (Fig. S6†). Such a high ratio of capacitive contribution leads to fast electrochemical kinetics for the Ni-HHTP-250 electrode, further confirming that the Ni-HHTP-250 electrode exhibits rapid electron and ion transport during the sodiation/desodiation processes.

Galvanostatic intermittent titration (GITT) is used to further evaluate the sodium-ion diffusion kinetics during the discharge/charge process (Fig. 5e). The Na$^+$ diffusion coefficients (D_{Na^+}) in the Ni-HHTP-250 electrode are calculated using the GITT method according to the following equation:[47]

$$D = \frac{4}{\pi \tau}\left(\frac{m_B V_M}{M_B S}\right)^2 \left(\frac{\Delta E_s}{\Delta E_t}\right)^2,$$

in which τ, m_B, V_M, S, and M_B are the pulse time (s), the real mass of the electrode (g), the molar volume (cm^3 mol^{-1}), the contact area between the electrode and the electrolyte, and the molecular weight (g mol^{-1}), respectively. Notably, the D_{Na^+} value during the sodium ion intercalation/extraction processes is about 10^{-11} cm^2 s^{-1}. Furthermore, EIS is used to assess the electrochemical performance of the Ni-HHTP-250 sample (Fig. 5f). The semicircle in the high-to-middle frequency region represents the electrochemical reaction kinetic process, ascribed to the charge-transfer resistance (R_{ct}). In addition, the inclined line in the low frequency region is defined as the Warburg impedance (Z_w), corresponding to the diffusion of sodium ions into the electrode. Using an equivalent circuit model of Zview software, the value of R_{ct} was estimated to be approximately 723.5 Ω. The values of R_{ct} are estimated to be approximately 1474, 1724 and 908.3 Ω for the Ni-HHTP electrode, the Ni-HHTP-160 electrode and the Ni-HHTP-340 electrode, respectively (Fig. S7a†). The Ni-HHTP-250 electrode has the smallest R_{ct} value among them, which indicates a fast charge transfer for the Ni-HHTP-250 electrode. Besides, EIS is also an important method for evaluating the diffusion coefficient of Na$^+$ ions within the particles. The diffusion coefficient of Na$^+$ ions was calculated and is shown in Table S1.† The D_{Na^+}

This journal is © the Partner Organisations 2023

Inorg. Chem. Front., 2023, **10**, 396–405 | **401**

value is the highest in the Ni-HHTP-250 electrode, indicating that the Ni-HHTP-250 electrode possesses the fastest reaction kinetics.

Charge storage mechanism

To further investigate the redox reaction mechanism of the Ni-HHTP-250 electrode in SIBs, *ex situ* FT-IR spectroscopy and XPS were performed at different charge/discharge states

during the 1st cycle. The results indicate that the Ni-HHTP-250 electrode undergoes both the conversion reaction of metal nodes and the insertion reaction of organic linkers. As shown in Fig. 6b, the peak of C=O at 1625 cm^{-1} weakens and the signal of the C–O group at 1250 cm^{-1} increases during the discharging process, and an opposite trend was found during the subsequent charging process, which indicates the transformation between the C=O and C–O groups. In addition, there are
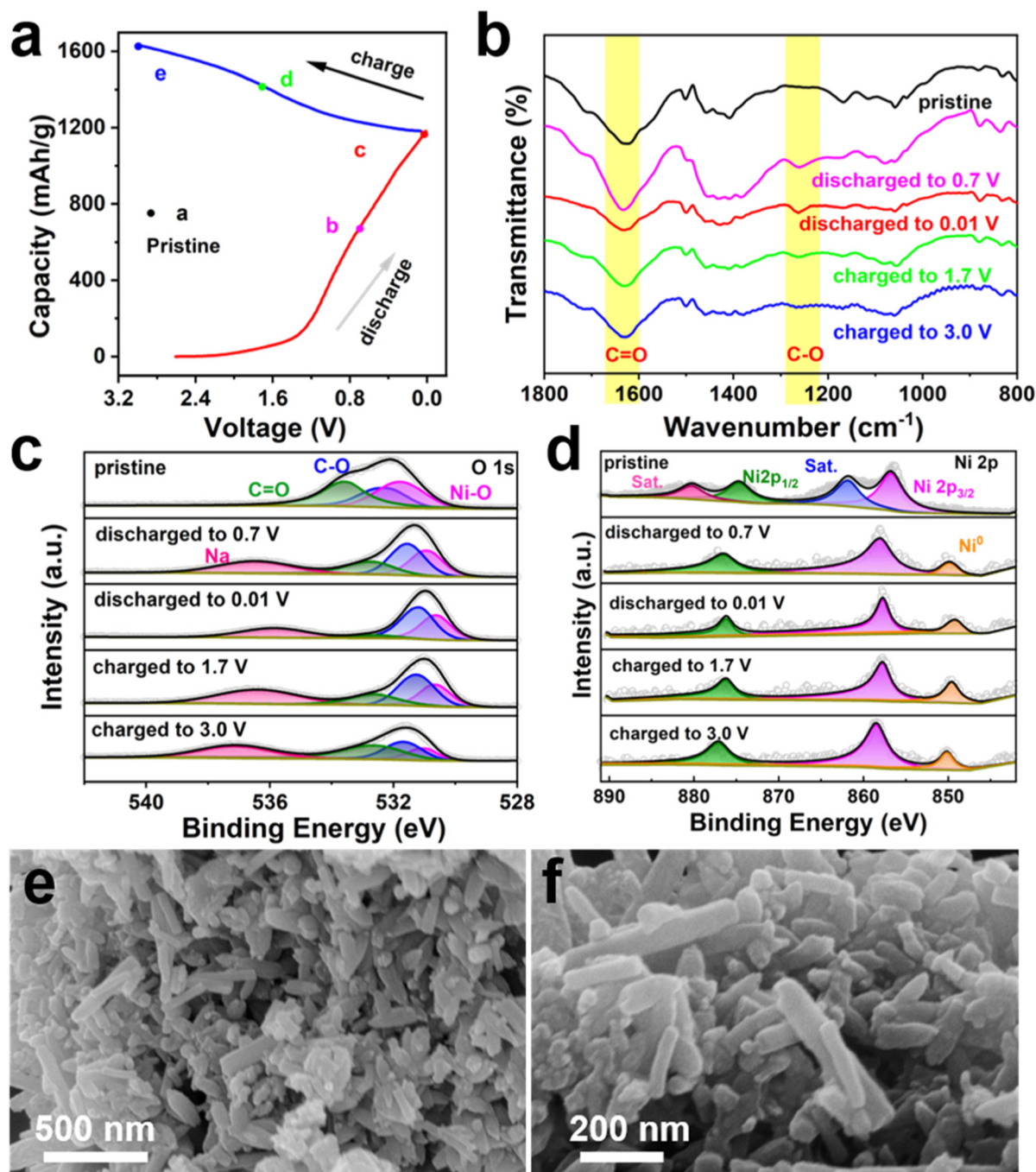

Fig. 6 The sodium storage mechanism of the Ni–HHTP-250 electrode. (a) Discharge/charge profiles at 200 mA g^{-1}. (b) *Ex situ* FT-IR spectra. (c) *Ex situ* XPS spectra of O 1s. (d) *Ex situ* XPS spectra of Ni 2p. (e and f) FESEM images at different magnifications of the Ni-HHTP-250 sample after 100 cycles.

no signals of Na$_2$O and NiO in the FT-IR spectra,[48] which indicates that the organic ligands are not decomposed. Furthermore, the structures of electrode materials after 100 cycles still remain as hexagonal nanorods (Fig. 6e and f), which also demonstrates that the frameworks are not destroyed. The XPS spectra of O 1s (Fig. 6c) also prove the above result. The C=O and C–O groups take part in the redox reaction. The *ex situ* XPS spectrum of Ni 2p in Ni-HHTP-250 (Fig. 6d) shows a pair of peaks at 856.7 eV (2p$_{3/2}$) and 874.7 eV (2p$_{1/2}$), along with two satellite peaks at 861.9 and 880.0 eV, both from Ni^{2+}. A signal peak of Ni (0) appears after discharging to 0.7 V. For Ni (0), the intensity of the peak after discharging to 0.7 V is lower than that of the peak after full discharge, which indicates that a part of Ni^{2+} is reduced to Ni (0) during the discharge process. During the charging process, parts of Ni (0) are oxidized to Ni^{2+} again. The phenomenon shows that the metal center also participates in the redox reaction. In conclusion, *ex situ* FT-IR spectroscopy and XPS indicate that both the metal center and C–O groups can store sodium ions during the charge/discharge process providing highly active sites for sodium storage. Based on the results of CV curves, *ex situ* FT-IR spectroscopy, XPS and FESEM, the Ni-HHTP electrode undergoes a conversion reaction to form Ni (0) and Na-HHTP in the first discharge reaction. Then, the Ni-HHTP electrode regenerates after the charge reaction.

Conclusions

In conclusion, we report an effective way to expose active sites. A series of Ni-HHTP samples with adjustable pores and highly exposed active sites with thermal treatment prior to carbonization were obtained. The Ni-HHTP-250 sample used as an electrode for SIBs delivers a large reversible discharge capacity of 420 mA h g^{-1} at 0.1 A g^{-1}. The excellent performance of the Ni-HHTP-250 sample can be attributed to the following advantages: (1) a 3D network structure formed by the cross-linked nanorods of lengths ranging from 200 nm to 1 μm will facilitate the permeation of the electrolyte and (2) the coexistence of micropores, mesopores and macropores is conducive to the insertion/extraction of sodium ions. The charge/discharge mechanism was also investigated. Both the metal ions and ligands are active sites for reversible reactions. After the electrochemical reaction, the morphology of the electrode was well maintained. This work gives a new route for enhancing the electrochemical performance of MOFs and deepens the study of the electrochemical reaction mechanism.

Author contributions

W. Shuang proposed conceptualization including ideas, formulation and evolution of overarching research goals and aims with the guidance of Z. Y. Bai and L. Yang; W. Shuang and Y. Wang performed the experiments and data analysis, and wrote the original draft; F. Y. Chen and Y. J. Wu contribu-

ted to the synthesis; and Z. Y. Bai and L. Yang gave suggestions and instructions to perform experiments. All authors contributed to the general discussion.

Conflicts of interest

There are no conflicts to declare.

Acknowledgements

References

1 M. D. Slater, D. Kim, E. Lee and C. S. Johnson, Sodium-Ion Batteries, *Adv. Funct. Mater.*, 2013, **23**, 947–958.

2 S. Chu and A. Majumdar, Opportunities and challenges for a sustainable energy future, *Nature*, 2012, **488**, 294–303.

3 G. Assat and J.-M. Tarascon, Fundamental understanding and practical challenges of anionic redox activity in Li-ion batteries, *Nat. Energy*, 2018, **3**, 373–386.

4 Y. Jiang, D. Song, J. Wu, Z. Wang, S. Huang, Z. Chen, B. Zhao and J. Zhang, Sandwich-like SnS$_2$/Graphene/SnS$_2$ with Expanded Interlayer Distance as High-Rate Lithium/Sodium-Ion Battery Anode Materials, *ACS Nano*, 2019, **13**, 9100–9111.

5 W. M. Seong, K. H. Cho, J. W. Park, H. Park, D. Eum, M. H. Lee, I. S. Kim, J. Lim and K. Kang, Controlling Residual Lithium in High-Nickel (>90%) Lithium Layered Oxides for Cathodes in Lithium-Ion Batteries, *Angew. Chem., Int. Ed.*, 2020, **59**, 18662–18669.

6 Y. Yang, M. Luo, Y. Xing, S. Wang, W. Zhang, F. Lv, Y. Li, Y. Zhang, W. Wang and S. Guo, A Universal Strategy for Intimately Coupled Carbon Nanosheets/MoM Nanocrystals (M = P, S, C, and O) Hierarchical Hollow Nanospheres for Hydrogen Evolution Catalysis and Sodium-Ion Storage, *Adv. Mater.*, 2018, **30**, 1706085.

7 T. Yu, Z. Zhao, L. Liu, S. Zhang, H. Xu and G. Yang, TiC$_3$ Monolayer with High Specific Capacity for Sodium-Ion Batteries, *J. Am. Chem. Soc.*, 2018, **140**, 5962–5968.

8 M. Yao, H. Wang, R. Qian, T. Yao and Y. Cheng, Robust hollow TiO$_2$ spheres for lithium/sodium ion batteries with excellent cycling stability and rate capability, *Inorg. Chem. Front.*, 2021, **8**, 5024–5033.

9 T. Huang, G. Du, Y. Qi, J. Li, W. Zhong, X. Zhang and M. Xu, A Prussian blue analogue as a long-life cathode for liquid-state and solid-state sodium-ion batteries, *Inorg. Chem. Front.*, 2020, **7**, 3938–3944.

This journal is © the Partner Organisations 2023

Inorg. Chem. Front., 2023, **10**, 396–405 | **403**

10 N. C. Burtch, H. Jasuja and K. S. Walton, Water Stability and Adsorption in Metal–Organic Frameworks, *Chem. Rev.*, 2014, **114**, 10575–10612.

11 H. C. Zhou, J. R. Long and O. M. Yaghi, Introduction to Metal–Organic Frameworks, *Chem. Rev.*, 2012, **112**, 673–674.

12 S. M. Cohen, Postsynthetic Methods for the Functionalization of Metal–Organic Frameworks, *Chem. Rev.*, 2012, **112**, 970–1000.

13 Z. Chang, D. H. Yang, J. Xu, T. L. Hu and X. H. Bu, Flexible Metal–Organic Frameworks: Recent Advances and Potential Applications, *Adv. Mater.*, 2015, **27**, 5432–5441.

14 N. Li, R. Feng, J. Zhu, Z. Chang and X.-H. Bu, Conformation versatility of ligands in coordination polymers: From structural diversity to properties and applications, *Coord. Chem. Rev.*, 2018, **375**, 558–586.

15 B. M. Connolly, D. G. Madden, A. E. H. Wheatley and D. Fairen-Jimenez, Shaping the Future of Fuel: Monolithic Metal–Organic Frameworks for High-Density Gas Storage, *J. Am. Chem. Soc.*, 2020, **142**, 8541–8549.

16 R.-B. Lin, S. Xiang, W. Zhou and B. Chen, Microporous Metal-Organic Framework Materials for Gas Separation, *Chem*, 2020, **6**, 337–363.

17 M. H. Teplensky, M. Fantham, C. Poudel, C. Hockings, M. Lu, A. Guna, M. Aragones-Anglada, P. Z. Moghadam, P. Li, O. K. Farha, S. Bernaldo de Quirós Fernández, F. M. Richards, D. I. Jodrell, G. Kaminski Schierle, C. F. Kaminski and D. Fairen-Jimenez, A Highly Porous Metal-Organic Framework System to Deliver Payloads for Gene Knockdown, *Chem*, 2019, **5**, 2926–2941.

18 A. Das, N. Anbu, M. Sk, A. Dhakshinamoorthy and S. Biswas, A functionalized UiO-66 MOF for turn-on fluorescence sensing of superoxide in water and efficient catalysis for Knoevenagel condensation, *Dalton Trans.*, 2019, **48**, 17371–17380.

19 Z. Li, X. Ge, C. Li, S. Dong, R. Tang, C. Wang, Z. Zhang and L. Yin, Rational Microstructure Design on Metal–Organic Framework Composites for Better Electrochemical Performances: Design Principle, Synthetic Strategy, and Promotion Mechanism, *Small Methods*, 2020, **4**, 1900756.

20 J. Liu, D. Xie, X. Xu, L. Jiang, R. Si, W. Shi and P. Cheng, Reversible formation of coordination bonds in Sn-based metal-organic frameworks for high-performance lithium storage, *Nat. Commun.*, 2021, **12**, 3131.

21 Y. Chen, M. Tang, Y. Wu, X. Su, X. Li, S. Xu, S. Zhuo, J. Ma, D. Yuan, C. Wang and W. Hu, A One-Dimensional π–d Conjugated Coordination Polymer for Sodium Storage with Catalytic Activity in Negishi Coupling, *Angew. Chem., Int. Ed.*, 2019, **58**, 14731–14739.

22 X. Yin, L. P. Lv, X. Tang, X. Chen, W. Sun and Y. Wang, Designing cobalt-based coordination polymers for high-performance sodium and lithium storage: from controllable synthesis to mechanism detection, *Mater. Today Energy*, 2020, **17**, 100478.

23 Y. Zhang, S. Yang, X. Chang, H. Guo, Y. Li, M. Wang, W. Li, L. Jiao and Y. Wang, MOF based on a longer linear ligand: electrochemical performance, reaction kinetics, and use as a novel anode material for sodium-ion batteries, *Chem. Commun.*, 2018, **54**, 11793–11796.

24 L. Wang, Y. Ni, X. Hou, L. Chen, F. Li and J. Chen, A Two-Dimensional Metal–Organic Polymer Enabled by Robust Nickel–Nitrogen and Hydrogen Bonds for Exceptional Sodium-Ion Storage, *Angew. Chem., Int. Ed.*, 2020, **59**, 22126–22131.

25 T. Chen, X. Liu, Y. Gong, C. Li, S. Xu and L. Plan, Recent progress on metal–organic framework-derived materials for sodium-ion battery anodes, *Inorg. Chem. Front.*, 2020, **7**, 567–582.

26 D. Yan and L. Pan, A new sodium storage mechanism of TiO_2 for sodium ion batteries, *Inorg. Chem. Front.*, 2016, **3**, 464–468.

27 S. Fan, S. Huang, Y. Chen, Y. Shang, Y. Wang, D. Kong, M. E. Pam, L. Shi, Y. W. Lim, Y. Shi and H. Y. Yang, Construction of complex NiS multi-shelled hollow structures with enhanced sodium storage, *Energy Storage Mater.*, 2019, **23**, 17–24.

28 N. Shi, B. Xi, M. Huang, J. Feng and S. Xiong, Hierarchical Octahedra Constructed by Cu_2S/MoS_2⊂Carbon Framework with Enhanced Sodium Storage, *Small*, 2020, **16**, 2000952.

29 X. Xu, J. Liu, J. Liu, L. Ouyang, R. Hu, H. Wang, L. Yang and M. Zhu, A General Metal-Organic Framework (MOF)-Derived Selenidation Strategy for In Situ Carbon-Encapsulated Metal Selenides as High-Rate Anodes for Na-Ion Batteries, *Adv. Funct. Mater.*, 2018, **28**, 1707573.

30 N. Contreras-Pereda, S. Pané, J. Puigmartí-Luis and D. Ruiz-Molina, Conductive properties of triphenylene MOFs and COFs, *Coord. Chem. Rev.*, 2022, **460**, 214459.

31 T. Pan, Y. Shen, P. Wu, Z. Gu, B. Zheng, J. Wu, S. Li, Y. Fu, W. Zhang and F. Huo, Thermal Shrinkage Behavior of Metal–Organic Frameworks, *Adv. Funct. Mater.*, 2020, **30**, 2001389.

32 M. Hmadeh, Z. Lu, Z. Liu, F. Gándara, H. Furukawa, S. Wan, V. Augustyn, R. Chang, L. Liao, F. Zhou, E. Perre, V. Ozolins, K. Suenaga, X. Duan, B. Dunn, Y. Yamamto, O. Terasaki and O. M. Yaghi, New Porous Crystals of Extended Metal-Catecholates, *Chem. Mater.*, 2012, **24**, 3511–3513.

33 H. Yoon, S. Lee, S. Oh, H. Park, S. Choi and M. Oh, Synthesis of Bimetallic Conductive 2D Metal–Organic Framework (Co_xNi_y-CAT) and Its Mass Production: Enhanced Electrochemical Oxygen Reduction Activity, *Small*, 2019, **15**, 1805232.

34 D. Xu, Z. Cao, Z. Ye, H. Zhang, L. Wang, M. John, P. Dong, S. Gao, J. Shen and M. Ye, Electrochemical oxidation of π-π coupling organic cathode for enhanced zinc ion storage, *Chem. Eng. J.*, 2021, **417**, 129245.

35 X. Riart-Ferrer, P. Sang, J. Tao, H. Xu, L. M. Jin, H. Lu, X. Cui, L. Wojtas and X. P. Zhang, Metalloradical activation of carbonyl azides for enantioselective radical aziridination, *Chem*, 2021, **7**, 1120–1134.

36 Y. Wu, Y. Zhang, Y. Chen, H. Tang, M. Tang, S. Xu, K. Fan, C. Zhang, J. Ma, C. Wang and W. Hu, Heterochelation

404 | *Inorg. Chem. Front.*, 2023, **10**, 396–405

This journal is © the Partner Organisations 2023

boosts sodium storage in π-d conjugated coordination polymers, *Energy Environ. Sci.*, 2021, **14**, 6514–6525.

37 L. Guo, J. Sun, X. Sun, J. Zhang, L. Hou and C. Yuan, Construction of 1D conductive Ni-MOF nanorods with fast Li$^+$ kinetic diffusion and stable high-rate capacities as an anode for lithium ion batteries, *Nanoscale Adv.*, 2019, **1**, 4688–4691.

38 W. Sun, S. Chen and Y. Wang, A metal–organic-framework approach to engineer hollow bimetal oxide microspheres towards enhanced electrochemical performances of lithium storage, *Dalton Trans.*, 2019, **48**, 2019–2027.

39 S. Gu, Z. Bai, S. Majumder, B. Huang and G. Chen, Conductive metal–organic framework with redox metal center as cathode for high rate performance lithium ion battery, *J. Power Sources*, 2019, **429**, 22–29.

40 M. Du, Q. Li and H. Pang, Oxalate-derived porous prismatic nickel/nickel oxide nanocomposites toward lithium-ion battery, *J. Colloid Interface Sci.*, 2020, **580**, 614–622.

41 S. Maiti, A. Pramanik and U. Manju, $Cu_3(1,3,5-benzenetricarboxylate)_2$ metal-organic framework: A promising anode material for lithium-ion battery, *Microporous Mesoporous Mater.*, 2016, **226**, 353–359.

42 B. Wang, Y. F. Zhang, J. He and C. C. Li, Dual-Redox Sites Guarantee High-Capacity Sodium Storage in Two-Dimension Conjugated Metal–Organic Frameworks, *Adv. Funct. Mater.*, 2022, **32**, 2112072.

43 C. Dong and L. Xu, Cobalt- and Cadmium-Based Metal–Organic Frameworks as High Performance Anodes for Sodium Ion Batteries and Lithium Ion Batteries, *ACS Appl. Mater. Interfaces*, 2017, **9**, 7160–7168.

44 J. Park, M. Lee, D. Feng, Z. Huang, A. C. Hinckley, A. Yakovenko, X. Zou, Y. Cui and Z. Bao, Stabilization of Hexaaminobenzene in a 2D Conductive Metal–Organic Framework for High Power Sodium Storage, *J. Am. Chem. Soc.*, 2018, **140**, 10315–10323.

45 P. Lou, Z. Cui, Z. Jia, J. Sun, Y. Tan and X. Guo, Monodispersed Carbon-Coated Cubic NiP_2 Nanoparticles Anchored on Carbon Nanotubes as Ultra-Long-Life Anodes for Reversible Lithium Storage, *ACS Nano*, 2017, **11**, 3705–3715.

46 F. Wan, L. Zhang, X. Dai, X. Wang, Z. Niu and J. Chen, Aqueous rechargeable zinc/sodium vanadate batteries with enhanced performance from simultaneous insertion of dual carriers, *Nat. Commun.*, 2018, **9**, 1656.

47 Y. Yun, B. Xi, F. Tian, W. Chen, W. Sun, H. Pan, J. Feng, Y. Qian and S. Xiong, Zero-Strain Structure for Efficient Potassium Storage Nitrogen-Enriched Carbon Dual-Confinement CoP Composite, *Adv. Energy Mater.*, 2021, **12**, 2103341.

48 M.-T. Li, J.-W. Sun, L. Yi Fei, M.-H. Niu, H.-Y. Zou, D.-Q. Sun and Y. Yu, POM-based metal organic frameworks with a woven fabric structure for lithium storage, *CrystEngComm*, 2022, **24**, 1279–1284.

This journal is © the Partner Organisations 2023

Inorg. Chem. Front., 2023, **10**, 396–405 | **405**